Water Resources Research

RESEARCH ARTICLE
10.1029/2022WR032307

Key Points:

- Density-driven flow modeling using a double control-volume-finite element method
- Dynamic mesh optimization applied to the Elder problem for several Rayleigh numbers with ×16 and ×6 speedup obtained respectively for low and high Rayleigh number 2D cases
- Extension of the unstable high Rayleigh number 2D Elder problem to three dimensions and demonstration of new 3D transient solutions, representing combinations of the previously observed, steady-state 2D solutions, as well as a unique, late-time, steady-state 3D solution

Correspondence to:
M. L. Bahlali,
m.bahlali@imperial.ac.uk

Citation:
Bahlali, M. L., Salinas, P., & Jackson, M. D. (2022). Efficient numerical simulation of density-driven flows: Application to the 2- and 3-D Elder problem. *Water Resources Research*, *58*, e2022WR032307. https://doi.org/10.1029/2022WR032307

Received 4 MAR 2022
Accepted 4 AUG 2022

Efficient Numerical Simulation of Density-Driven Flows: Application to the 2- and 3-D Elder Problem

Meissam L. Bahlali[1], Pablo Salinas[1], and Matthew D. Jackson[1]

[1]Department of Earth Science and Engineering, Novel Reservoir Modelling and Simulation Group, Imperial College London, London, UK

Abstract Modeling density-driven flow in porous media is challenging due to the nonlinear coupling between flow and transport equations, the large domains of interest and the wide range of time and space scales involved. Solving this type of problem numerically using a fixed mesh can be prohibitively expensive. Here, we apply a dynamic mesh optimization (DMO) technique along with a control-volume-finite element method to simulate density-driven flows. DMO allows the mesh resolution and geometry to vary during a simulation to minimize an error metric for one or more solution fields of interest, refining where needed and coarsening elsewhere. We apply DMO to the Elder problem for several Rayleigh numbers. It is demonstrated that DMO accurately reproduces the unique two-dimensional (2D) solutions for low Rayleigh number cases at significantly lower computational cost compared to an equivalent fixed mesh, with speedup of order ×16. For unstable, high Rayleigh number 2D cases, multiple steady-state fingering solutions exist and are all captured by our approach with high accuracy and significantly reduced computational cost, with speedup of order ×6. Velocity-dependent dispersion is shown to have a small impact on the 2D numerical solutions. The lower computational cost of simulations using DMO allows extension of the high Rayleigh number case to a three dimensional (3D) configuration. We demonstrate new 3D fingering patterns that have not been observed previously. Early time, transient 3D patterns represent combinations of the previously observed, steady-state 2D solutions, but all evolve to a single, steady-state finger in the late time limit.

1. Introduction

Density-driven flows in porous media are frequently encountered in natural systems and are caused by fluid density gradients that typically arise in response to changes in fluid temperature or composition. Density-driven flows have significant economic and environmental impacts, and numerical modeling is often used to predict their behavior for risk assessment, reservoir characterization or management. However, the highly non-linear nature of the coupling between fluid density and temperature and/or composition can lead to the formation of physical instabilities that are extremely challenging to capture in numerical models.

The Elder problem is one example of a density-driven flow that exhibits physical instabilities. It was originally observed in thermal convection experiments in porous media (Elder, 1967) and has since been extensively studied (Elder et al., 2017; Johannsen, 2003; Prasad & Simmons, 2003; Thorne & Sukop, 2004; Van Reeuwijk et al., 2009; Voss & Souza, 1987). The original Elder experiment induced thermal convection in a rectangular Hele-Shaw cell by heating the central half of the base of the cell. The thermal Elder problem was adapted by Voss and Souza (1987) for the analogous problem of solute transport in a two-dimensional (2D), water-saturated porous medium, by inverting the geometry and injecting more dense saltwater into a domain filled with less dense freshwater via the central half of the top of the domain. The solute problem is mathematically equivalent to its thermal convection counterpart via the Rayleigh number, which is the key parameter characterizing the various flow behaviors observed in the Elder problem. The Rayleigh number represents the ratio between the flux caused by density differences and the flux caused by diffusion and, for the solute problem, is expressed as

$$Ra = \frac{gk\alpha\rho_0(\Delta c)H}{\phi\mu D_0}, \tag{1}$$

where μ is the fluid viscosity, k is the magnitude of the isotropic permeability tensor, ρ_0 is the reference fluid density, ϕ is porosity, D_0 is the reference Fickian diffusion coefficient, Δc is the variation in solute concentration between upper and lower boundaries, α is the coefficient of proportionality relating fluid density and solute concentration, H is the vertical dimension and g is the acceleration due to gravity. Equation 1 is trivially modified

10.1029/2022WR032307

for the equivalent thermal problem, replacing Δc by the temperature difference, ρ_0 by the reference fluid temperature, D_0 by the reference Fourier diffusion coefficient and α by the coefficient of linear thermal expansion.

In Elder problem cases with sufficiently low Rayleigh number ($Ra < 76$), the existence of a unique steady-state solution has been demonstrated (Johannsen, 2003; Van Reeuwijk et al., 2009). For $Ra > 76$, there are multiple steady-state solutions. Numerical simulation of the Elder problem with very large Rayleigh number (of order $Ra = 400$, which has been studied previously) is very challenging because solutions are highly unstable, exhibiting multiple convection plumes (alternatively referred to as fingers) depending on numerical parameters such as the numerical discretization scheme, grid or mesh resolution and timestep size (Ackerer & Younes, 2008; Frolkovič & De Schepper, 2000; Johannsen, 2003; Van Reeuwijk et al., 2009; Woods & Carey, 2007; Woods et al., 2003; Younes & Ackerer, 2010). In the $Ra = 400$ Elder problem, three different steady-state solutions comprising one ("S1"), two ("S2") or three ("S3") separate fingers have been reported and it has been suggested that at least two of these solutions should be accurately reproduced by a numerical code for it to be sufficiently verified for the Elder problem (Van Reeuwijk et al., 2009). Johannsen (2002) noted that S1 and S2 solutions are frequently observed in numerical simulations, while S3 may be found by choosing suitable initial conditions; these observations have been confirmed by Van Reeuwijk et al. (2009). Other parameters such as the mesh resolution, numerical scheme and formulation of the governing equations may also be responsible for the generation of one of the three patterns (Diersch & Kolditz, 2002; Park & Aral, 2007; Van Reeuwijk et al., 2009; Woods & Carey, 2007).

To capture the unstable movement of the convection plumes and the narrow transition zones between the fingers, high mesh resolution is essential, which means that simulations are computationally expensive, even for the 2D Elder problem. Most simulations of density-driven flows of environmental relevance require 3D models, often of a large domain, in which case computations that properly resolve density-driven instabilities are prohibitively expensive, despite the increasing uptake of high-performance computing (HPC) (Ackerer & Younes, 2008; Künze, 2014; Künze & Lunati, 2012; Lunati & Jenny, 2008; Younes & Ackerer, 2010).

To address this issue, here we use an advanced dynamic mesh optimization (DMO) approach to obtain numerical solutions with high accuracy but lower computational cost compared to using a static mesh. DMO has been extensively used in inertia-dominated flows (e.g., Aristodemou et al., 2018; Piggott et al., 2009; Viré et al., 2012; Yang et al., 2016; Zheng et al., 2015); applications have been much more limited in porous media flow modeling (Hamzehloo et al., 2021; Jackson et al., 2015; Kampitsis et al., 2020; Mostaghimi et al., 2014, 2015; Obeysekara et al., 2018; Salinas et al., 2021). In the present work, both the stable and unstable Elder problems are investigated; to our knowledge, this is the first study to investigate the use of DMO for the Elder problem.

The DMO approach we use here allows elements within an unstructured mesh to be split or amalgamated (h-adaptivity), or element vertices to be moved (r-adaptivity). It differs significantly from the related concept of adaptive grid refinement (AGR), which has previously been applied to model reservoir flows, although not to simulations of the Elder problem. AGR utilizes only h-adaptivity and Cartesian grids (Dahle et al., 1990, 1992; Hornung & Trangenstein, 1997; Schmidt & Jacobs, 1988; Trangenstein, 2002; Wolff et al., 2013).

DMO allows the mesh resolution to change during a simulation, to minimize an error metric for one or more solution fields of interest such as pressure, temperature and solute concentration. In practice, this means that higher (and often anisotropic) mesh resolution is used in regions where the chosen solution fields have steep gradients, and lower resolution is used elsewhere. Previous work has shown that DMO can be used to obtain high resolution numerical results for the analogous Saffman-Taylor instability, at much lower computational cost than an equivalent fixed mesh (Kampitsis et al., 2020; Mostaghimi et al., 2016). We hypothesize here that DMO can similarly be used to obtain high resolution results for the Elder problem at lower computational cost than equivalent fixed mesh simulations.

The equations governing density-driven flow are solved here on an unstructured, dynamically changing tetrahedral mesh using a double control-volume-finite element method (DCVFEM) which, along with the DMO algorithm, is implemented in the open-source Imperial College Finite Element Reservoir SimulaTor (IC-FERST). In the DCVFEM, velocity is discretized using Finite Elements (FE) while pressure and conserved properties such as heat and solute concentration are discretized using Control Volumes (CV). The DCVFEM is used here because it has been shown to be robust despite the use of highly distorted meshes; such meshes may be created to represent

Table 1
Parameters Used in the Elder Problem, Following Voss and Souza (1987)

Parameter	Value
Molecular diffusion coefficient [m^2/s]	3.565×10^{-6}
Solutal expansion coefficient	0.2
Permeability [m^2]	1×10^{-30} ($Ra = 0$)
	4.845×10^{-13} ($Ra = 60, 400$)
Porosity	0.1
Freshwater density [kg/m^3]	1,000
Saltwater density [kg/m^3]	1,200
Gravitational acceleration [m/s^2]	9.81
Longitudinal dispersivity [m]	0, 0.05, 0.5
Transverse dispersivity [m]	0, 0.005, 0.05

complex geological geometries or flow features in groundwater and other geologically heterogeneous subsurface reservoir models, and can be created during application of DMO (Salinas, Pavlidis, Xie, Jacquemyn, et al., 2017).

The paper is organized as follows. In Section 2, we briefly present the concepts of DMO and the DCVFEM used here, before describing the Elder problem configuration. Section 3 reports tests of our computational framework against benchmark solutions based on the stable (Ra = 0, Ra = 60) and unstable (Ra = 400) Elder problem, along with a computational performance analysis. In Section 3.4 we take advantage of the significant reduction in computational cost offered by DMO and demonstrate application of our framework in a 3D implementation of the Elder problem, observing new solutions that have not been reported previously. Finally, Section 4 draws conclusions.

2. Method

2.1. Governing Equations

The governing equation for single-phase, density-dependent flow in porous media is the generalized form of Darcy's law, written as

$$\mathbf{q} = \frac{-\mathbf{k}}{\mu}(\nabla p - \rho \mathbf{g}) \tag{2}$$

where $\mathbf{q}$ is the Darcy velocity vector defined as $\mathbf{q} = \phi \mathbf{v}$ in which ϕ is the porosity and $\mathbf{v}$ is the mean pore water velocity vector, $\mathbf{k}$ denotes the permeability tensor, μ and ρ denote the dynamic viscosity and density of the fluid, respectively, and $\mathbf{g}$ is the gravitational field tensor.

The continuity equation is defined as

$$\frac{\partial \phi \rho}{\partial t} + \nabla \cdot (\phi \rho \mathbf{v}) = 0, \tag{3}$$

Invoking the Boussinesq approximation, Equation 3 simplifies to

$$\nabla \cdot \mathbf{v} = 0 \ . \tag{4}$$

For the Elder problem and, more generally, for any passive scalar, the transport equation for the solute concentration field C is described by

$$\frac{\partial \phi \rho C}{\partial t} + \nabla \cdot (\phi \rho \mathbf{v} C) = \nabla \cdot [\phi \rho (D_m \mathbf{I} + \mathbf{D}) \cdot \nabla C] \tag{5}$$

where $\mathbf{I}$ is the identity tensor, D_m is the molecular diffusion coefficient and $\mathbf{D}$ is the dispersion coefficient tensor. Dispersion is a mechanical phenomenon that arises from the random variations of the velocity field due to the structure of the porous medium. In the present work, it is approximated by an isotropic formulation (Hamzehloo et al., 2021). Invoking the Boussinesq approximation, Equation 5 simplifies to

$$\frac{\partial C}{\partial t} + (\mathbf{v} \cdot \nabla) \ C = \nabla \cdot [(D_m \mathbf{I} + \mathbf{D}) \cdot \nabla C] \ . \tag{6}$$

Density variations are computed using a linear relationship between density and solute (salt) concentration (Croucher & O'Sullivan, 1995)

$$\rho = \rho_0(1 + \alpha C) \tag{7}$$

where ρ_0 = 1,000 kg/m^3 is the corresponding reference density for pure water with $C = 0$ and α is chosen to yield ρ = 1,200 kg/m^3 for the maximum solute concentration C_m used in the modeling (see Table 1).

We express results in terms of normalized solute mass fraction, defined as

$$c = \frac{C}{C_m} \quad . \tag{8}$$

2.2. Numerical Approach

The governing equations are discretized using the DCVFEM, originally introduced by Salinas, Pavlidis, Xie, Jacquemyn, et al. (2017) and based on the family of control volume finite element methods (Abushaikha et al., 2017; Durlofsky, 1993; Forsyth, 1991; Geiger et al., 2004; Helmig & Huber, 1998; Salinas et al., 2018; Xie et al., 2016). In conventional CVFEM, pressure and velocity are discretized using finite elements (Gomes et al., 2017). However, solving the pressure equation using this type of formulation is challenging on distorted meshes, which are frequently encountered within the high aspect ratio domains associated with geological and hydrological models: the pressure solution may fail to converge or be physically unrealistic (Salinas, Pavlidis, Xie, Jacquemyn, et al., 2017). The DCVFEM tackles this issue by discretizing pressure using control volumes (Gomes et al., 2017; Jackson et al., 2015; Salinas, Pavlidis, Xie, Jacquemyn, et al., 2017).

We use the element pair $P_{n-1}(DG)P_n(CV)$, where P_{n-1} represents the polynomial order of velocity discretization, DG denotes the Discontinuous Galerkin method, P_n refers to the polynomial order of pressure and concentration discretization, and CV stands for the control volume shape functions. Here, $n = 1$, that is, velocity is discontinuous and is represented FE-wise with a discretization order of 0, while pressure and concentration are continuous and are represented CV-wise with a discretization order of 1.

Time is discretized using an implicit θ-method, where θ varies between 0.5 (Crank-Nicholson) and 1 (implicit Euler), based on a total variation diminishing approach (Gomes et al., 2017).

The coupled system of discretized equations is solved using a Picard iterative method (Anderson, 1965) as described in Salinas, Pavlidis, Xie, Adam, et al. (2017). The coupled solutions for pressure and concentration are iterated by the Picard solver until the concentration field has converged within a user-defined tolerance between two consecutive non-linear iterations. Then, time advances by one time-level until the final time is reached. In the present work, the convergence criteria for the non-linear solver is for the infinite norm of the normalized difference between two non-linear iterations of the concentration field to be below 0.05, with a maximum of 20 non-linear iterations per time-level. An adaptive time stepping is used, which ensures that if convergence is not achieved, the time step is reduced and the process repeated. Conversely, if the non-linear solver converges very efficiently, the time step is increased for the next time-level.

2.3. Dynamic Mesh Optimization

The dynamic mesh optimization algorithm has been described previously (Adam et al., 2016; Jackson et al., 2015; Pain et al., 2001) so only a brief summary is provided here. We use an anisotropic DMO approach, implementing *hr*-adaptivity in which elements can be split and amalgamated, and element edges and vertices can be moved, in order to produce meshes which provide the desired solution precision. The method is summarized as follows:

1. An approximation is calculated of the local interpolation error **E** between the smooth field of interest $\phi(x_i)$ and its linear interpolation over the finite element mesh $\phi = \sum_i q^i N_i$, where N_i are the finite element basis functions and q^i the nodal values of the field. Cea's lemma shows that **E** is bounded by a function of the following Hessian matrix **H**,

$$\mathbf{H} = \begin{bmatrix} \frac{\partial^2 \phi}{\partial x_1^2} & \frac{\partial^2 \phi}{\partial x_1 \partial x_2} & \cdots & \frac{\partial^2 \phi}{\partial x_1 \partial x_\delta} \\ \frac{\partial^2 \phi}{\partial x_2 \partial x_1} & \frac{\partial^2 \phi}{\partial x_2^2} & \cdots & \frac{\partial^2 \phi}{\partial x_2 \partial x_\delta} \\ \vdots & \vdots & \ddots & \vdots \\ \frac{\partial^2 \phi}{\partial x_\delta \partial x_1} & \frac{\partial^2 \phi}{\partial x_\delta \partial x_2} & \cdots & \frac{\partial^2 \phi}{\partial x_\delta^2} \end{bmatrix}, \tag{9}$$

where δ denotes the dimension of the problem; $\delta = 2$ or 3 in the test cases shown here.

Entries E_{ij} of the local interpolation error **E** are given by

10.1029/2022WR032307

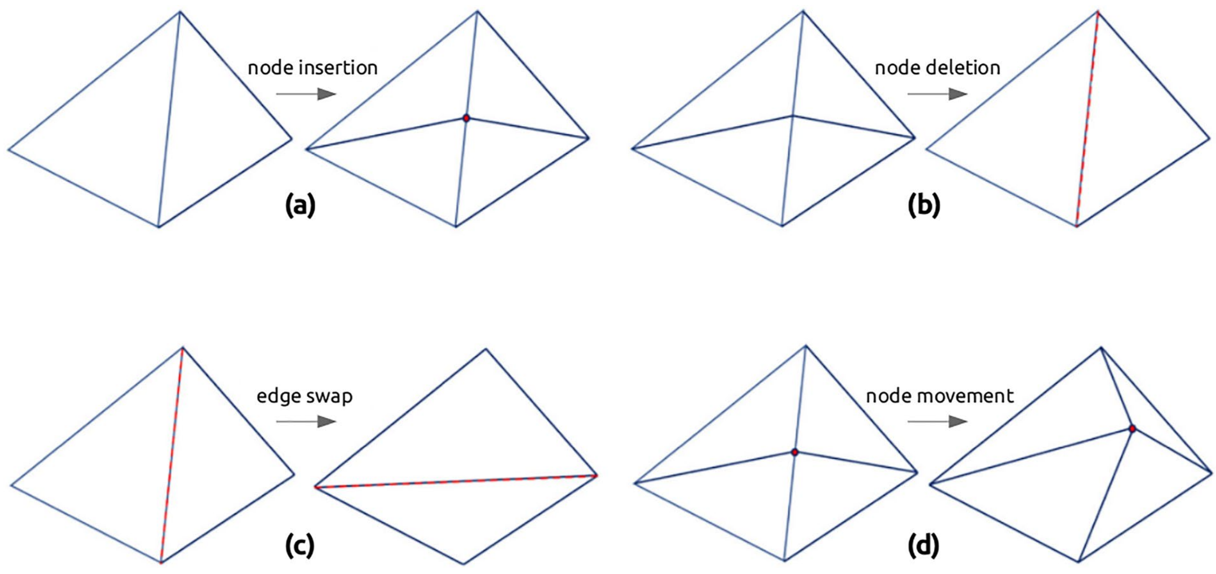

Figure 1. Allowed mesh adaptivity operations: (a) node insertion, (b) node deletion, (c) edge swap, and (d) node movement (Pain et al., 2001).

$$E_{ij} = \mathbf{det}(\mathbf{H})^{\left(\frac{1}{2\gamma\delta}\right)} \frac{|H_{ij}|}{\xi}, \tag{10}$$

where ξ is the degree of the polynomial of the norm used ($\xi = 1$ in the simulations shown here) and γ is the user-specified precision for the solution field.

2. A functional I, based on the interpolation error $\mathbf{E}$, is then calculated to measure the solution quality, given by

$$I = \sum_{i \in edges} \left(e_i^t \mathbf{E} e_i - 1\right)^2 \tag{11}$$

where e_i denote the vectors describing the element edge length on the finite element mesh. I is calculated for each finite element.

3. A new mesh is generated that minimizes I by applying the following operations (Pain et al., 2001):
   - Edge splitting: refinement via splitting existing elements and adding additional nodes along existing edges.
   - Edge collapse: coarsening via removing existing nodes and replacing two nodes by a single node lying at the edge midpoint.
   - Edge and face-edge swapping: reordering the connectivity of existing elements and introducing an edge between the two nodes of two elements that are not shared.
   - Node movement: re-positioning nodes within the convex hull spanned by the elements which share it.

   Element by element, these four mesh operations (Figure 1) are applied sequentially to create a new mesh achieving uniform quality elements and the desired precision. After each local transformation of the mesh, the maximum functional I is calculated and the mesh transformation is accepted if

$$\max_{e' \in S'} I_{e'} - \max_{e \in S} I_e \leq -\kappa \tag{12}$$

$$\max_{e \in S} I_e > I_t, \tag{13}$$

   where e and e' denote elements, and S and S' denote sets of elements, respectively, before and after the proposed local mesh transformation. κ and I_t are, respectively, a user defined smallness parameter and functional threshold value. Here we use $\kappa = 0.01$ and $I_t = 0.15$ (Pain et al., 2001).

   The mesh optimization process is also constrained by user-defined limits such as maximum and minimum edge length, number of elements, element anisotropy and gradation, which specifies the length-scale over which element edge lengths can change, to allow sharp changes in edge length or enforce a more gradual change in edge length.

10.1029/2022WR032307

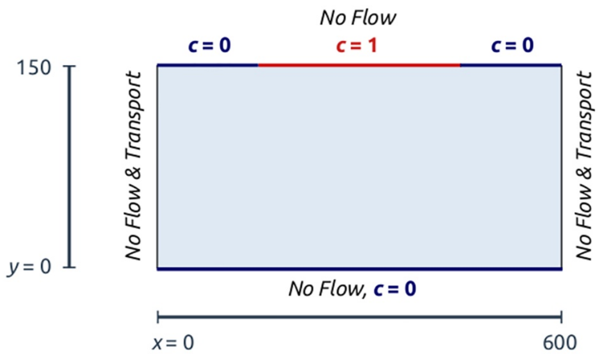

(a) 2D Elder problem. Dimensions are in meters.

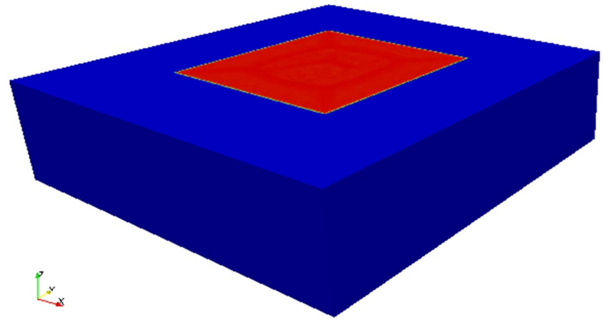

(b) 3D Elder problem. Model dimensions are the same as in (a), and extended in the third dimension.

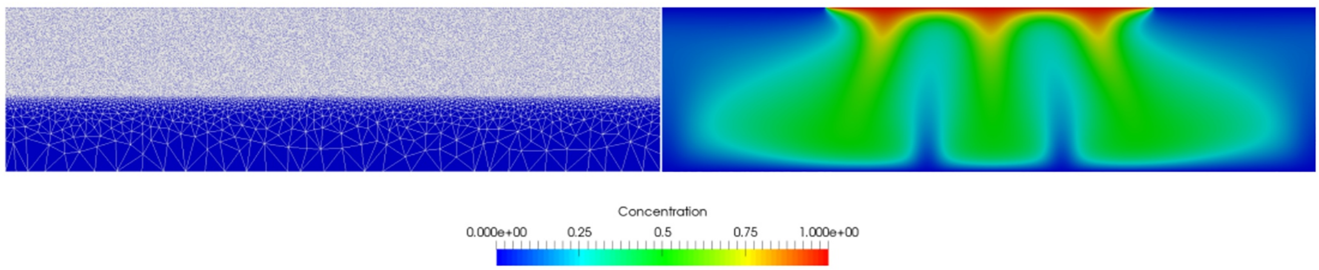

(c) Homogeneous (left) and heterogeneous (right) initial concentration for the 2D Ra=400 Elder problem. The initial mesh is also shown on the left figure. The heterogeneous initial condition is similar to the one used by Van Reeuwijk et al. (2009).

Figure 2. Schematic of the (a) 2D Elder problem and (b) 3D Elder problem. Panel (c) shows the imposed initial conditions for the 2D $Ra = 400$ case.

4. The solution fields are interpolated from the old mesh to the new mesh using a conservative Galerkin projection (Adam et al., 2016; Farrell & Maddison, 2011).

2.4. Method Evaluation

The above-described method was applied to the Elder problem, by first studying the original 2D problem (Figure 2a). This consists of a 2D rectangular geometry containing a homogeneous and isotropic porous medium, initially saturated with fresh (pure) water. All boundaries except the upper boundary are sealed (no flow or transport). In the central part of the upper boundary, there is a source of a highly saline brine ($c = 1$, $\rho = 1{,}200$ kg/m^3 [Voss & Souza, 1987]), while a Dirichlet condition of zero concentration ($c = 0$, $\rho = 1{,}000$ kg/m^3) is imposed on the left and right parts of the same boundary as well as the bottom boundary (Elder, 1967; Van Reeuwijk et al., 2009). For the 2D $Ra = 0$ and $Ra = 60$ cases, a homogeneous initial condition for concentration was used ($c = 0$). For the $Ra = 400$ case, two types of initial conditions were tested (Figure 2c): homogeneous ($c = 0$) and a heterogeneous S3-shaped concentration, following the approach of Van Reeuwijk et al. (2009). We discuss the motivation for using the heterogeneous initial condition later in Section 3.2. Model parameters are shown in Table 1. The purely diffusive case $Ra = 0$ was obtained by setting a very low permeability (1×10^{-30} m^2). The $Ra = 60$ case was obtained by reducing the imposed concentration at the central part of the top boundary condition to $c = 0.15$. Dispersivity was ignored in all cases, except when its impact was specifically investigated in Section 3.2.1 (see Table 1).

We then extended the 2D $Ra = 400$ Elder problem to 3D by considering a rectangular parallelepiped, at the top of which the saline brine is injected through a square at the center of the surface boundary (Figure 2b). The other parameters are the same as for the 2D model.

We began by simulating the purely diffusive case $Ra = 0$, comparing our results against the semi-analytical solution of Van Reeuwijk et al. (2009). We next considered the $Ra = 60$ case, for which benchmark numerical solutions are available (Van Reeuwijk et al., 2009). We then considered the $Ra = 400$ case in 2D, before analyzing the computational costs of fixed mesh and DMO cases. We finished by demonstrating application of DMO in the $Ra = 400$ case in 3D.

Where applied, DMO was triggered every time step and adapted the mesh based on the concentration field by imposing an absolute error tolerance of $\gamma = 0.0009$. The specified mesh gradation value was 1.5. The adaptive mesh resolution was controlled by changing the minimum element edge length $h_{\min}$ whilst holding the maximum edge length $h_{\max}$ fixed. Here, in all cases, $h_{\max} = 80$ m. $h_{\min}$ as well as the corresponding number of elements for each test case are shown in Table 2. In simulations using DMO, $h_{\min}$ denotes the average element edge length. Solutions obtained using a fixed mesh and DMO with the same $h_{\min}$ can therefore be directly compared, as they have the same spatial resolution. The number of elements in DMO simulations varies as the simulation progresses, and the number reported in Table 2 corresponds to the time-weighted average over the duration of the simulation.

For the $Ra = 400$ case, the mesh was initially fixed to allow the fingers to grow, following the approach used by Kampitsis et al. (2020) for viscous fingering. A fine mesh was used around the saltwater inflow boundary, with the same edge length as the minimum edge length specified for DMO, and covering a large enough portion of the domain to resolve the early growth of the fingers (see Figure 2c). A coarse mesh was used elsewhere. The mesh was fixed for a period corresponding to 2% of the total simulation time, to allow the fingers to grow; the mesh was therefore fixed for 1.5 years for both the 2D and 3D cases, after which DMO was activated.

Unless otherwise stated in Table 2, a Courant-Friedrichs-Lewy (CFL) number of 1 was used, which specifies the maximum timestep; smaller timesteps are allowed if required for convergence. Consistent with previous studies, the simulations were run for 200 years for the $Ra = 0$ and $Ra = 60$ cases (Papaspyros et al., 2016; Van Reeuwijk et al., 2009), while a simulation time of 75 years was chosen for the 2D and 3D cases with $Ra = 400$.

3. Results

3.1. Purely Diffusive Case $Ra = 0$ and Low Rayleigh Number Case $Ra = 60$

Three cases were studied for each value of Ra ($Ra = 0$ cases are termed "PureDiff" while $Ra = 60$ cases are termed "LowRa") with different fixed and adaptive mesh resolutions (cases 1–3; Table 2). Figure 3 shows a time snapshot of concentration contours at $t = 200$ years, predicted here for $Ra = 0$ and $Ra = 60$ using the finest mesh resolution tested (Case 3) with both a fixed mesh and DMO. Also shown are the published benchmark results of Van Reeuwijk et al. (2009) for both $Ra = 0$ and $Ra = 60$ cases. There is an excellent match for both values of Ra and for both fixed mesh and DMO simulations. Increasing Ra from zero to 60 yields a steeper density gradient between top and bottom boundaries and evidence for incipient finger formation at the upper boundary (compare Figures 3a and 3b).

The comparisons against the published benchmark data of Van Reeuwijk et al. (2009) are qualitative, so we also conducted a mesh refinement analysis to demonstrate convergence for the $Ra = 0$ case, varying $h_{\min}$ and plotting the concentration integral versus the time-averaged number of elements (Figure 3c). We use the concentration integral to measure the quality of the results as the lower the precision, the more artificial diffusion is introduced, bringing in more concentration; in summary, a lower precision implies a higher value of the concentration integral. The concentration integral is defined in its discretized form as

$$c_{integral} = \sum_{i=1}^{N_{CV}} c_i \; V_i, \tag{14}$$

Table 2
Summary of Simulation Cases and Fingering Patterns Obtained for the Ra = 400 Cases

Case	h_{min} (m)	Number of elements	
		Fixed	DMO
(a) 2D Elder problem—$Ra = 0$ and $Ra = 60$			
2D-PureDiff-1 and 2D-LowRa-1	0.75	423,412	21,621 and 25,224
2D-PureDiff-2 and 2D-LowRa-2	1.0	238,218	17,740 and 22,392
2D-PureDiff-3 and 2D-LowRa-3	1.25	152,428	15,246 and 20,227

Case	h_{min} (m)	Number of elements		Fingering pattern	
				CFL	
		Fixed	DMO	1	0.01
(b) 2D Elder problem—$Ra = 400$					
2D-HighRa-0 (S3-shaped initial condition)	0.55	785,710	85,554	S3	n/a
2D-HighRa-1	0.55	785,710	105,264	Hybrid S3-S2-S1	Hybrid S3-S2-S1
2D-HighRa-2	0.75	423,412	81,322	Hybrid S3-S2-S1	S2
2D-HighRa-3	1	238,218	62,545	S2	S2
2D-HighRa-4	3	27,125	n/a	S2	S2
2D-HighRa-5	4	15,144	n/a	S1	S1
2D-HighRa-6	5	9,402	n/a	S2	S2
2D-HighRa-7	6	6,684	n/a	S2	S2
2D-HighRa-8	8	3,648	n/a	Hybrid S3-S2-S1	Hybrid S3-S2-S1
2D-HighRa-9	10	2,362	n/a	S2	S2
2D-HighRa-10	12	1,690	n/a	S2	S2
2D-HighRa-11	15	1,032	n/a	Hybrid S3-S2-S1	Hybrid S3-S2-S1
2D-HighRa-12	17	884	n/a	Hybrid S3-S2-S1	Hybrid S3-S2-S1
2D-HighRa-13	21	604	n/a	S1	S1
2D-HighRa-14	30	274	n/a	S2	S2
2D-HighRa-15	35	230	n/a	S1	S1
2D-HighRa-16	40	150	n/a	S1	S1

Case	h_{min} (m)	Number of elements		Fingering pattern
		Fixed	DMO	
(c) 3D Elder problem—$Ra = 400$				
3D-1	2	n/a	9,238,105	Hybrid S9-S6-S4-S1
3D-2	3	n/a	4,006,629	Hybrid S8-S4-S1
3D-3	5	n/a	1,415,903	Hybrid S7-S5-S1
3D-4	8	n/a	478,255	Hybrid S7-S5-S1
3D-5	15	n/a	93,233	Hybrid S7-S6-S4-S1
3D-6	20	n/a	42,379	Hybrid S7-S5-S4-S1
3D-7	35	n/a	8,213	S1
3D-8	40	n/a	5,690	S1

Note. h_{min} stands for the minimum edge length bound (mesh size constraint).

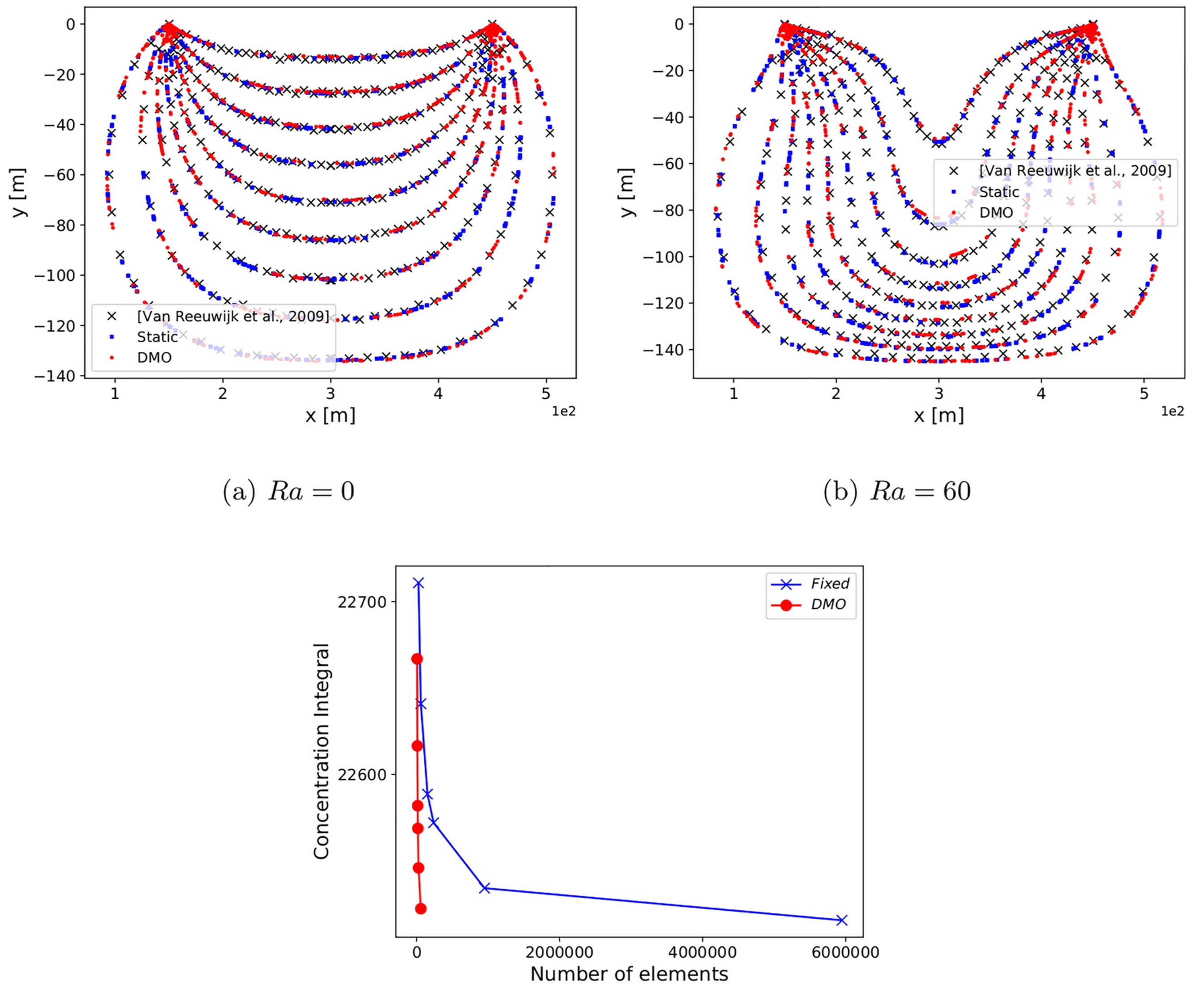

(a) $Ra = 0$ (b) $Ra = 60$

(c) Concentration integral

Figure 3. Steady-state solutions of the Elder problem for (a) $Ra = 0$ and (b) $Ra = 60$, showing concentration contours for the fixed and dynamic mesh optimization (DMO) cases with the highest mesh resolution (cases 2D-PureDiff-3 and 2D-LowRa-3 in Table 2), and the benchmark results of Van Reeuwijk et al. (2009). Panel (c) shows numerical convergence of the $Ra = 0$ case, plotting concentration integral as a function of the time-averaged number of elements for both fixed mesh and DMO simulations. Each datapoint in (c) corresponds to a chosen value of $h_{\min}$.

where N_{CV} is the total number of control volumes, c_i is the concentration in control volume i and V_i is the volume of control volume i.

Fixed and DMO cases with the same $h_{\min}$ return similar values of concentration integral, but cases with DMO show much more rapid convergence. Consequently, a similar quality of solution is obtained by DMO, but using significantly fewer elements than the corresponding fixed mesh, leading to a lower computational cost. We return to this issue in Section 3.3.

DMO allows high solution accuracy to be maintained using fewer elements because the elements are no longer uniformly distributed across the domain, as they are in fixed mesh simulations (Figure 4). The mesh refines to capture the steeper concentrations fronts associated with the downwards propagating salinity front, and coarsens elsewhere. The mesh geometry therefore changes depending on the timestep (e.g., compare Figures 4a and 4k)

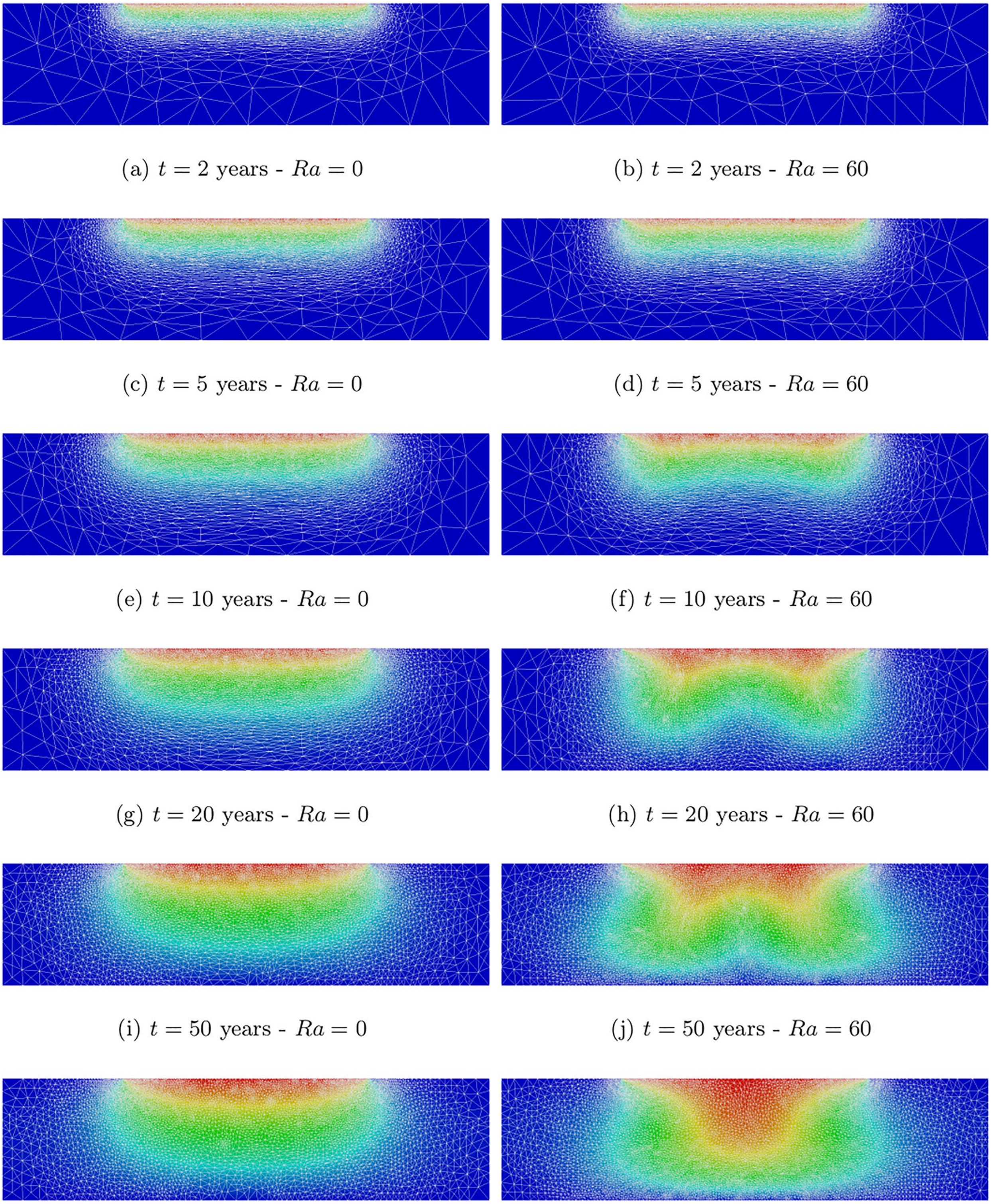

(a) $t = 2$ years - $Ra = 0$

(b) $t = 2$ years - $Ra = 60$

(c) $t = 5$ years - $Ra = 0$

(d) $t = 5$ years - $Ra = 60$

(e) $t = 10$ years - $Ra = 0$

(f) $t = 10$ years - $Ra = 60$

(g) $t = 20$ years - $Ra = 0$

(h) $t = 20$ years - $Ra = 60$

(i) $t = 50$ years - $Ra = 0$

(j) $t = 50$ years - $Ra = 60$

(k) $t = 200$ years - $Ra = 0$

(l) $t = 200$ years - $Ra = 60$

Figure 4. Time evolution of salt concentration and the dynamically adapting mesh for $Ra = 0$ (left) and $Ra = 60$ (right) from $t = 0$ to $t = 200$ years, for the 2D-PureDiff-3 and 2D-LowRa-3 cases in Table 2.

10.1029/2022WR032307

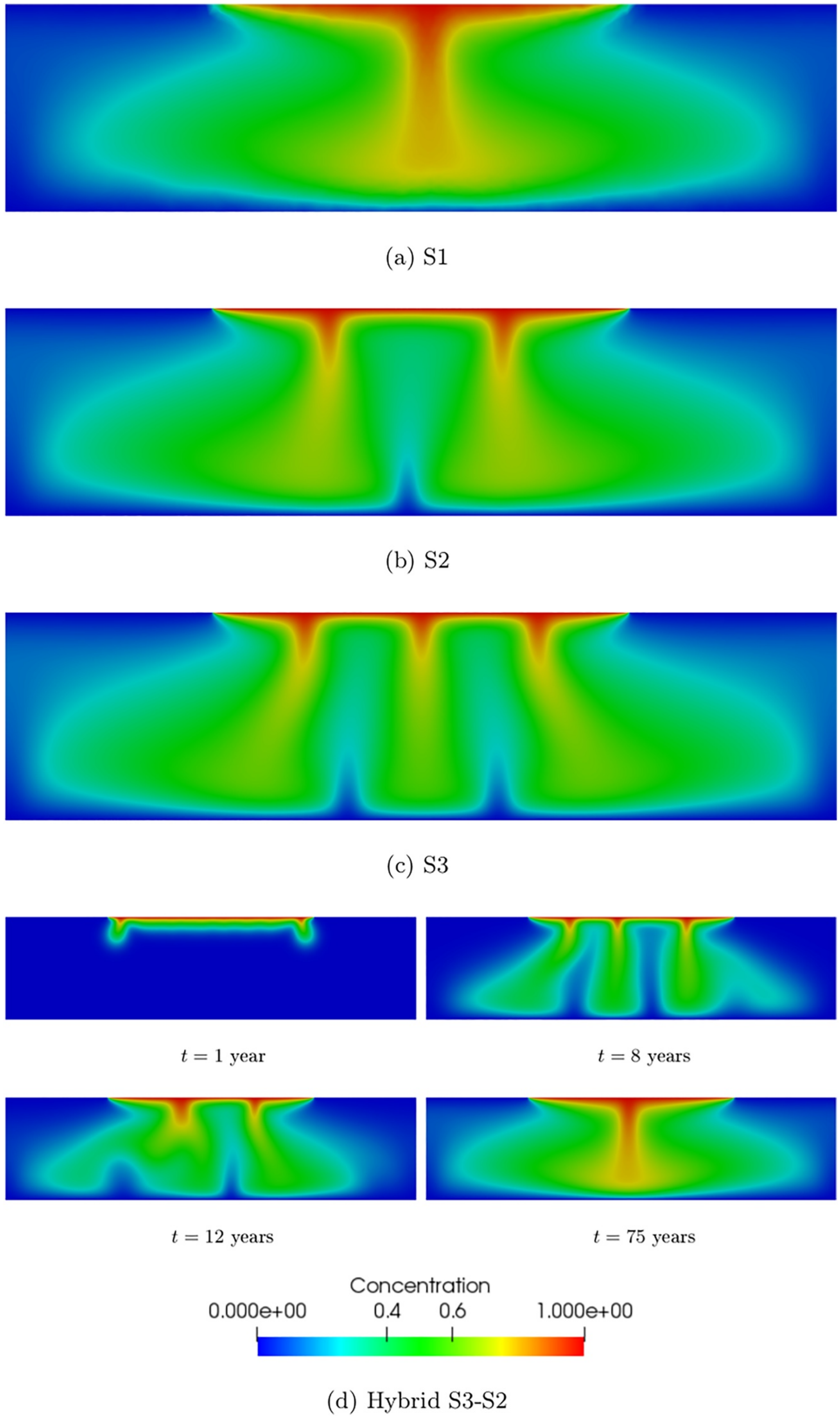

Figure 5. Salt concentration after $t = 70$ years, showing examples of the (a) S1, (b) S2, and (c) S3 fingering patterns, corresponding to Cases 2D-HighRa-8, 2D-HighRa-3 and 2D-HighRa-0 respectively in Table 2. Panel (d) shows the time evolution of the salt concentration for the hybrid Case 2D-HighRa-2 from $t = 2$ to $t = 75$ years. The simulation starts off with an S3 fingering pattern before two fingers begin to merge into one; this merged finger in turn merges with the third finger, finally leading to the S1 pattern. All results reported in this figure were obtained using a fixed mesh.

and the chosen Ra (e.g., compare Figures 4a–4c–4e–4g–4i–4k and Figures 4b–4d–4f–4h–4j–4l). We conclude that the $Ra = 0$ and $Ra = 60$ steady-state solutions are accurately reproduced, with and without DMO. We now study the unstable $Ra = 400$ problem.

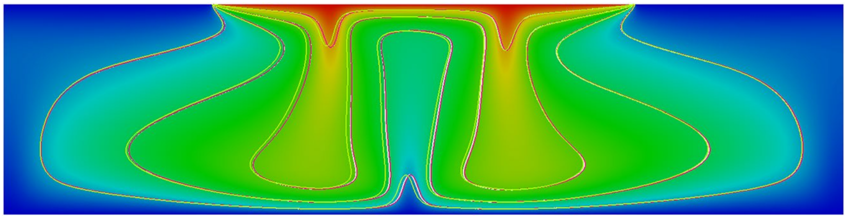

Figure 6. Salt concentration contours for dispersivity values of $\alpha_l = 0$ (white contours), 0.05 (pink contours) and 0.5 (green contours), for the $Ra = 400$ case 2D-HighRa-3 in Table 2, obtained using a fixed mesh.

3.2. High Rayleigh Number Case, $Ra = 400$

3.2.1. The 2D $Ra = 400$ Elder Problem on Unstructured Static Meshes

The $Ra = 400$ Elder problem in 2D exhibits at least three stable (denoted S1, S2, and S3) and eight unstable steady-state solutions (Frolkovič & De Schepper, 2000; Johannsen, 2002), which makes it less appropriate for benchmarking numerical models. Our aim here is to examine solutions to the $Ra = 400$ Elder problem obtained using fully unstructured static meshes.

We began by examining the 2D problem using the parameters reported in Table 1, varying the fixed mesh resolution by varying the minimum edge length ($h_{\min}$) and the timestep by varying the CFL number. For the finest mesh (Cases 2D-HighRa-0, 2D-HighRa-1), the initial condition was also varied by either considering a homogeneous ($c = 0$) or a heterogeneous (S3-shaped) initial concentration field (see Figure 2c and Table 2). We discuss the motivation for using the heterogeneous initial condition later in this section.

Considering the homogeneous initial condition for concentration, our first key observation is that the S1 and S2 stable fingering patterns were both captured irrespective of the mesh resolution. Examples of each pattern are shown in Figure 5. The S1 pattern has a single finger (Figure 5a); the S2 pattern has two fingers (Figure 5b). However, the S3 pattern, with three fingers, was not captured, although we found that it could be obtained by modifying the equation of state for density, restricting the density contrast to <10%, corresponding to a maximum density difference of 100 kg/m^3 rather than 200 kg/m^3. However, changing the density equation of state means that this is no longer a solution to the Elder problem.

Van Reeuwijk et al. (2009) demonstrated a clear difficulty in capturing the S3 pattern. They obtained S3 only by digitizing the S3 solution of Johannsen (2003) and using this as the initial condition. Thus, S3 was shown to be one of the steady-state solutions to the Elder problem, but only by imposing an S3-shaped pattern as an initial condition, suggesting that only a small subset of initial conditions lead to S3. This was our motivation for trying the heterogeneous S3-shaped initial condition for our simulation. In our case, the S3-shaped initial condition was the S3 steady-state solution obtained using the modified equation of state (Figure 2c, right). Using this specific heterogeneous S3-shaped initial condition yielded the steady-state S3 solution for the Elder problem (Figure 5c).

In our simulations, S3 also appears as a transient pattern in the so-called several "hybrid" patterns, in which the number of fingers varies during the simulation. An example hybrid S3-S2-S1 pattern is shown in Figure 5d; the solution initially has three fingers (see the snapshot at $t = 8$ years), but two of these later merge (snapshot at $t = 10$ years) to leave two fingers (snapshot at $t = 12$ years), which, in turn, merge, to finally leave a single finger (see the snapshot at $t = 75$ years).

The fingering patterns for each $Ra = 400$ simulation case are summarized in Table 2. In general, the fingering pattern changes from S1 to S2 with increasing mesh resolution, although there are several exceptions: for example, case 2D-HighRa-5 returns the S1 solution, even though the mesh resolution is finer than case 2D-HighRa-6 which returns the S2 pattern. Previous studies have also failed to demonstrate a consistent relationship between mesh resolution and fingering pattern. Moreover, the same fingering pattern for a given mesh resolution is usually obtained irrespective of the chosen CFL number; however, there are again several exceptions: for example, case 2D-HighRa-2 returns the S2 pattern with CFL = 0.01, but a hybrid S3-S2-S1 pattern with CFL = 1. Papaspyros et al. (2016) obtained the three S1, S2, and S3 patterns by changing the time step of the simulations, but other studies have found the link between timestep and fingering pattern to be

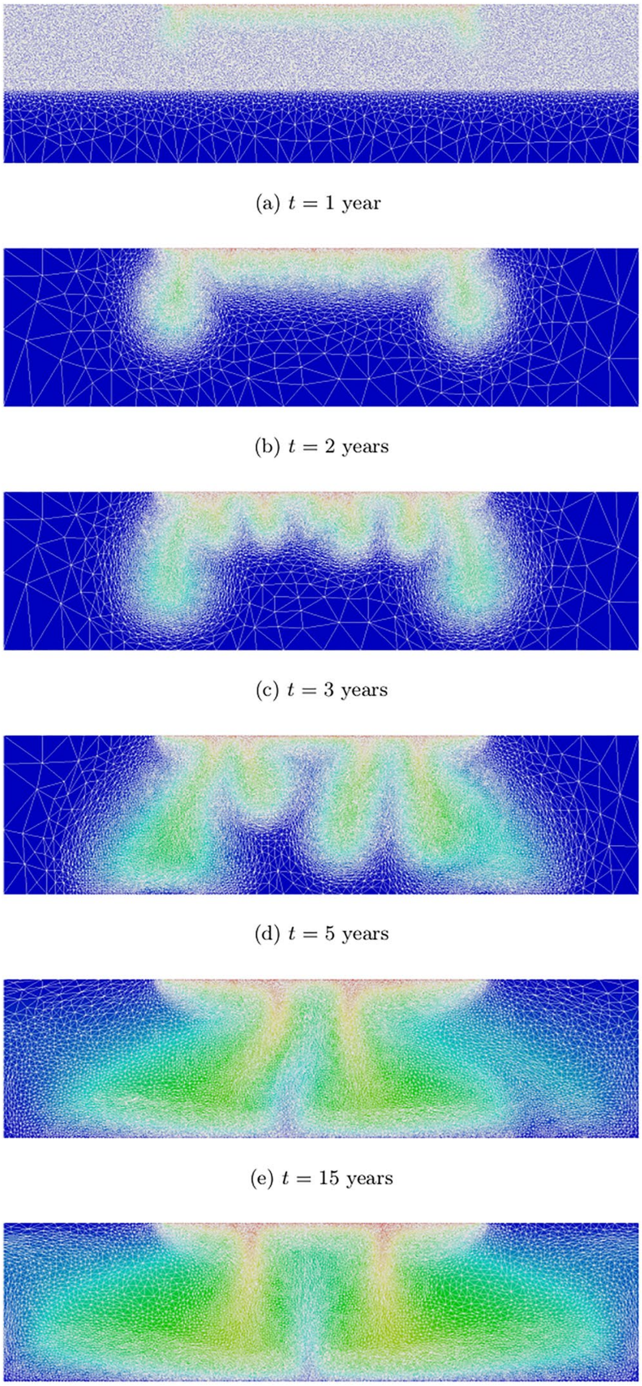

(a) $t = 1$ year

(b) $t = 2$ years

(c) $t = 3$ years

(d) $t = 5$ years

(e) $t = 15$ years

(f) $t = 75$ years

Figure 7. Time evolution of salt concentration and the dynamically adapting mesh for the $Ra = 400$ case from $t = 0$ to $t = 75$ years, for the case with the highest DMO mesh resolution (2D-HighRa-3 in Table 2).

less clear: Frolkovič and De Schepper (2000) used two different time steps and found no important visible differences; Woods and Carey (2007) used five different time steps and found that the fingering patter only differed significantly for the smallest timestep, while Younes and Ackerer (2010) studied several different implicit and explicit time stepping schemes and showed that temporal truncation error can have a significant effect on the results.

Our numerical framework also allows us to test the sensitivity of the unstable Elder problem to velocity-dependent dispersion, and we investigated the impact of three different longitudinal dispersivity values: $\alpha_l = 0$ (the original model), 0.05 and 0.5 (Table 1). The transverse dispersivity $\alpha_t = 0.1\alpha_l$. Figure 6 shows the salt concentration contours for each dispersivity tested after $t = 75$ years for the $Ra = 400$ Case 2D-HighRa-3 of Table 2. Velocity-dependent dispersion does not significantly affect the solutions, suggesting that the numerous previous numerical studies of the Elder problem have been reasonable in neglecting dispersion.

3.2.2. Dynamic Mesh Optimization for the 2D $Ra = 400$ Elder Problem

We now focus on DMO simulations for the 2D $Ra = 400$ Elder problem. Given that use of DMO should increase speed and/or accuracy by significantly reducing the number of elements, we chose to reproduce only the finest fixed mesh simulations corresponding to Cases 2D-HighRa-1, 2D-HighRa-2, and 2D-HighRa-3 in Table 2.

In Figure 7, the time evolution of the S3 fingering pattern corresponding to Case 2D-HighRa-3 (Table 2) is shown together with the corresponding dynamically adapting mesh. The initial fine mesh in the upper part of the domain has the same resolution as the corresponding fixed mesh and is held in place until $t = 1.5$ years, after which time DMO is activated. The fingering pattern and evolution is well captured by DMO, which places higher resolution in and around the fingers, and coarse resolution elsewhere, allowing the fingering pattern to be captured at high resolution but using fewer elements.

Figure 8 shows the salt concentration contours obtained with and without DMO at $t = 75$ years for the $Ra = 400$ test case and for all three tested values of the minimum element edge length (cases 2D-HighRa-0, 2D-HighRa-1, 2D-HighRa-2 and 2D-HighRa-3 in Table 2). The overall agreement between the static and DMO simulations is good. The small discrepancies in some parts of the domain are most likely due to perturbations brought about by DMO, which is here triggered every time step. DMO captures the key aspects of these complex fingering patterns, with significantly fewer elements (Table 2; note the reduction in elements from 7,85,710 to 1,05,264 for the fixed and DMO meshes in the highest resolution case 2D-HighRa-1).

3.3. Computational Performance Analysis of DMO

The results presented in the previous sections have demonstrated that DMO can produce solutions with the same accuracy as an equivalent fixed mesh but using far fewer elements (see Table 2). Here we demonstrate that the reduction in element numbers yields a similar reduction in computational cost, reporting a quantitative computational performance test for the $Ra = 0$, $Ra = 60$ and $Ra = 400$ cases.

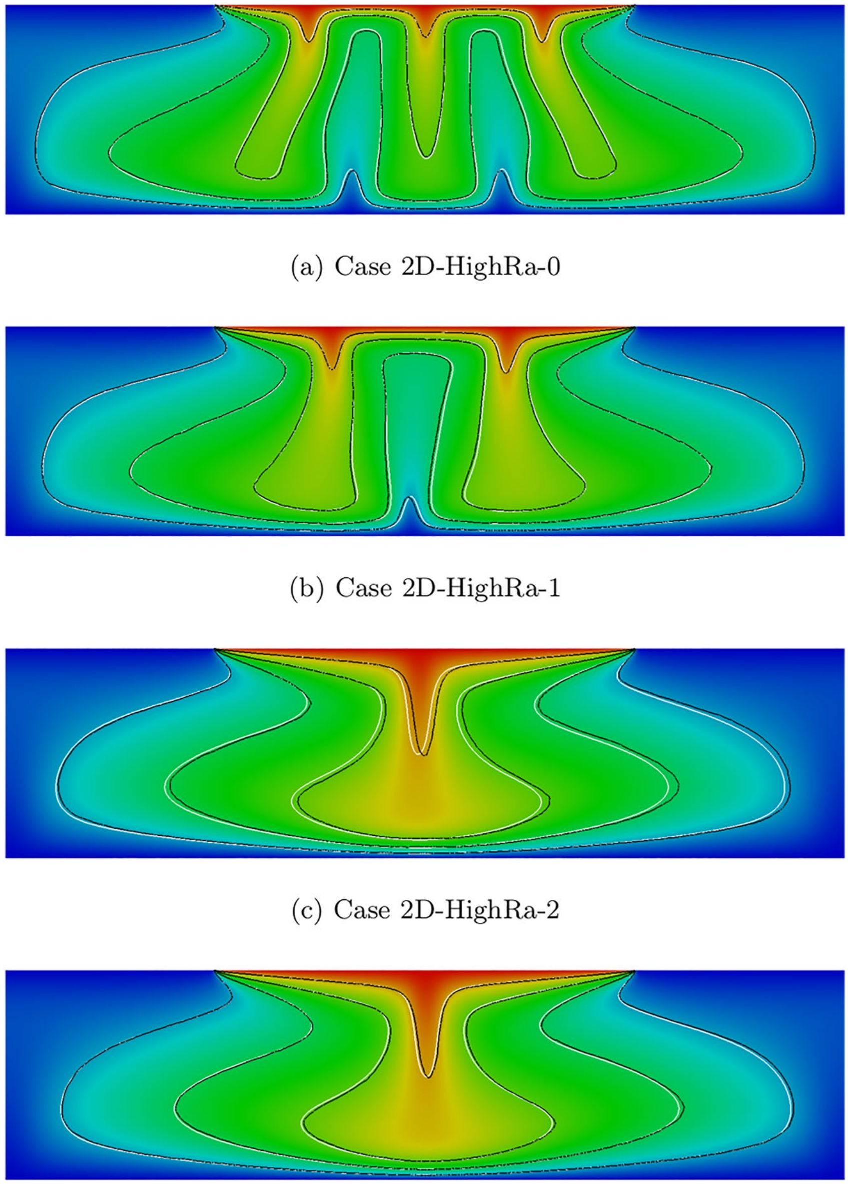

(a) Case 2D-HighRa-0

(b) Case 2D-HighRa-1

(c) Case 2D-HighRa-2

(d) Case 2D-HighRa-3

Figure 8. Salt concentration contours obtained with (black contours) and without (white contours) DMO at $t = 75$ years for $Ra = 400$ and all four Cases 2D-HighRa-0, 2D-HighRa-1, 2D-HighRa-2 and 2D-HighRa-3 in Table 2.

Figure 9a shows the normalized CPU time against the minimum element edge length for both the fixed mesh and DMO simulations. The CPU time is normalized by the time taken to run the fixed mesh simulation with the same minimum edge length. DMO simulations show significant speedup compared to fixed mesh simulations because they require fewer elements. The computational speedup is significantly improved even though DMO is triggered every time step and, in the $Ra = 400$ case, the initial mesh is kept fixed for 2% of the simulation time. Quantitatively, for the $Ra = 0$ case, the speedup is of order ×8.2, ×11.3, and ×16.5 for $h_{\text{cell,min}} = 1.25$ (Case 2D-PureDiff-3), 1 (Case 2D-PureDiff-2) and 0.75 m (Case 2D-PureDiff-1), respectively. For the $Ra = 60$ case, it is of order ×6.2, ×8.9, and ×15.4 for Case 2D-LowRa-3, Case 2D-LowRa-2 and Case 2D-LowRa-1, respectively. Finally, for the most challenging $Ra = 400$ case, the speedup is of order ×3.2, ×3.8, and ×6.8 for $h_{\text{cell,min}} = 1$ (Case 2D-HighRa-3), 0.75 (Case 2D-HighRa-2) and 0.55 m (Case 2D-HighRa-1), respectively.

10.1029/2022WR032307

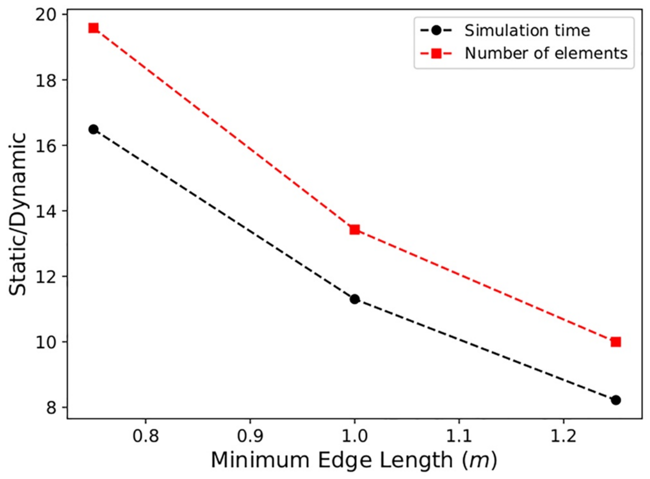

(a) Speedup - $Ra = 0$

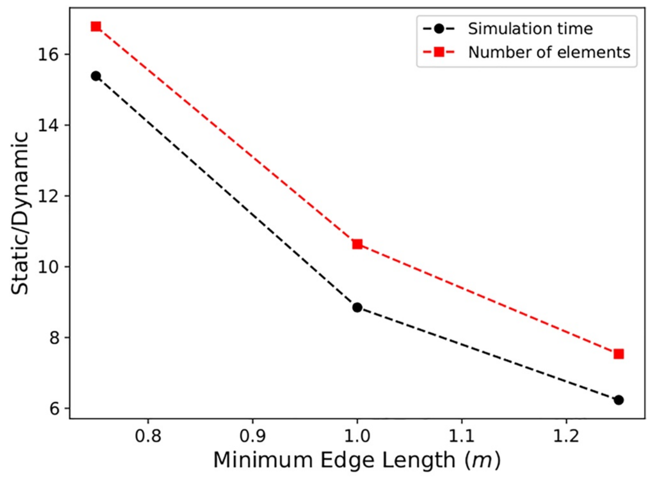

(b) Speedup - $Ra = 60$

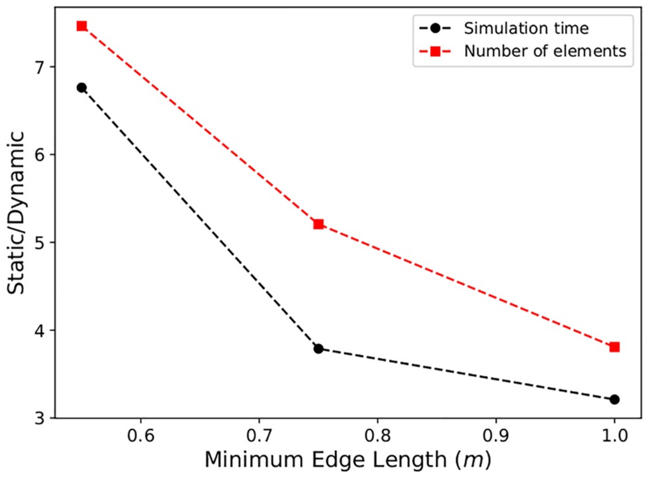

(c) Speedup - $Ra = 400$

Figure 9. Normalized CPU time (static/dynamic mesh) against the minimum element edge length. The CPU time is normalized by the time taken to run the fixed mesh simulation with the same minimum edge length.

DMO yields more significant speed-up in problems with a large number of fixed mesh elements, where the number of elements is large either because high mesh resolution is required, or because the model domain is large. So far, we have investigated the benefit of DMO only for the former case: high mesh resolution is required but the 2D model domain is small. In the next section, we use DMO to obtain high resolution results in a large model domain by extending the Elder problem into 3D which, to the best of our knowledge, is the first time this has been reported.

3.4. Application of DMO: A 3D Unstable Elder-Based Problem

Using DMO, our implementation of the 3D Elder problem (Figure 2b) requires about 9.2 million elements using the smallest minimum edge length tested ($h_{min} = 2$ m; see Table 2). Solving the same problem using a static mesh of the same resolution would require at least 50 million elements. Consequently, the 3D Elder problem is simu-

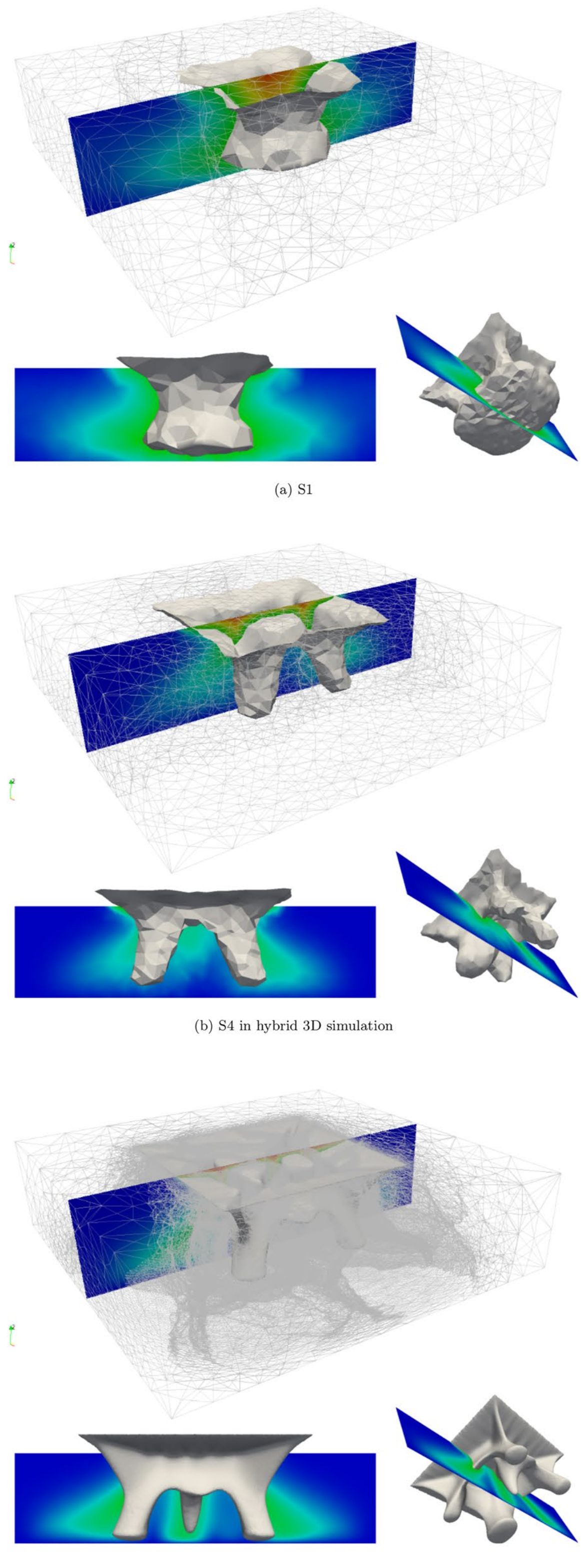

(a) S1

(b) S4 in hybrid 3D simulation

(c) S6 in hybrid 3D simulation

Figure 10. Perspective views of snapshots of numerical solutions of the 3D Elder problem, showing (a) S1 fingering pattern after 75 years (Case 3D-7), (b) S4 in hybrid fingering pattern after 9 years (Case 3D-6), and (c) S6 in hybrid fingering pattern after 9 years (Case 3D-1). Also shown is the corresponding mesh. The gray volumetric shape represents the $c = 0.5$ isosurface.

10.1029/2022WR032307

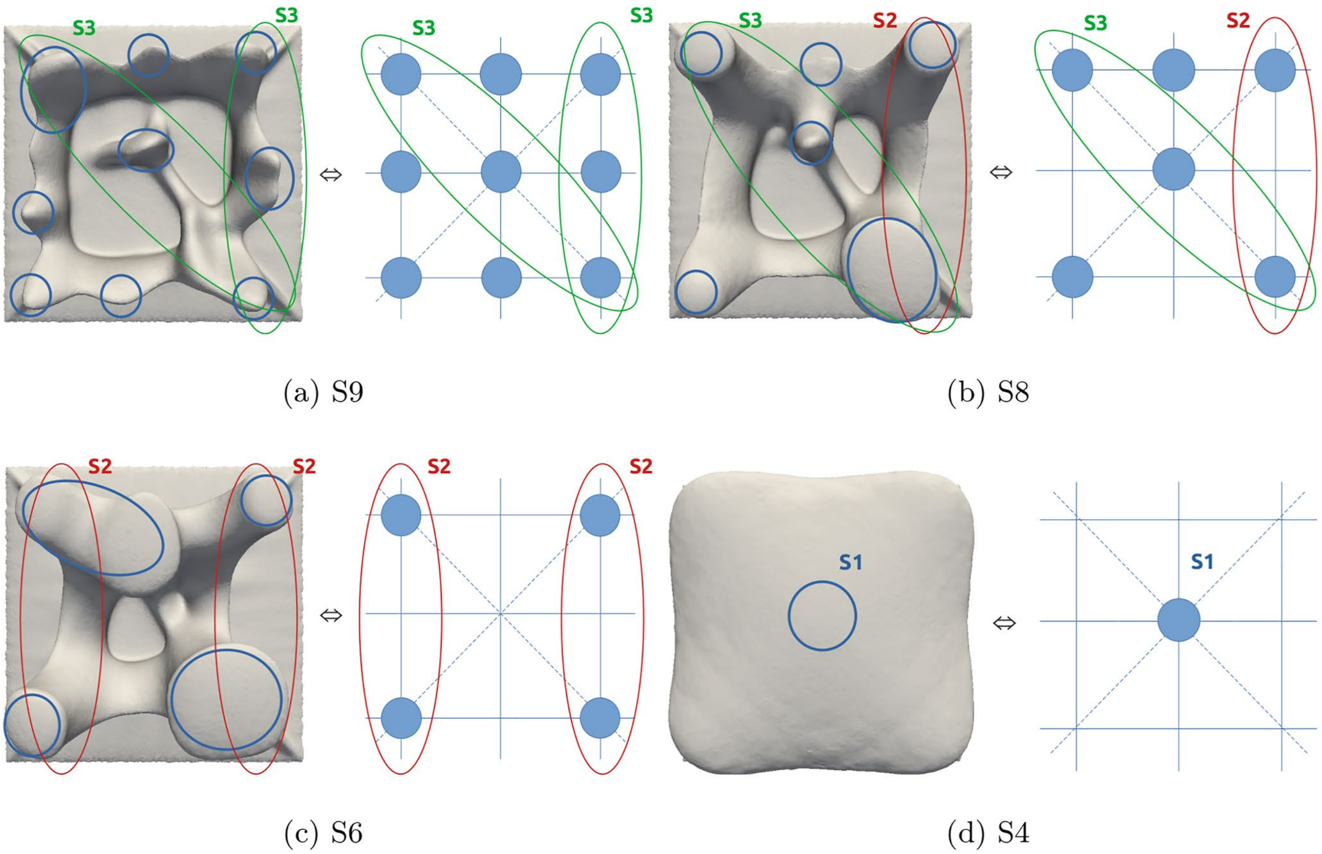

Figure 11. Plan view of each of the 3D fingering patterns observed, from (a) S9 to (f) S4. Each panel shows a snapshot of the numerical solution, visualizing the concentration $c = 0.5$ isosurface from below. The finger locations are indicated on the isosurface by the blue circles. Next to the snapshot is a simplified schematic of the fingering pattern in planview. Blue circles correspond to fingers. Colored ellipses indicate how the 3D fingering patterns represent combinations of the S1, S2, and S3 fingering patterns. Any vertical section through the 3D solution on the grid of lines shown in blue will return an S2 or S3 pattern. Snapshots taken from the hybrid Case 3D-2.

lated using DMO only; the aim of this paper is not to demonstrate use of high performance computing to simulate the 3D Elder problem. As for the 2D problem, we undertook a mesh sensitivity study by varying the minimum edge length (Table 2).

The 3D Elder problem shows fingering patterns that have not been reported previously. The S1 pattern is common to both 2D and 3D simulations (e.g., Figure 10a) and is in fact the only 3D stable solution (Table 2). We also observe much larger numbers of transient fingers, with patterns S2, S3, S4, S5, S6, S7, S8, S9 all produced at some time (Table 2). For example, Figure 10b shows the S4 pattern obtained at $t = 9$ years for Case 3D-6, and Figure 10c shows the S6 pattern obtained at $t = 9$ years for Case 3D-1. However, these patterns occur only in "hybrid" solutions. The 3D solutions show more merging of fingers, so solutions with a large initial number of fingers show a decrease in the number of fingers with time. The 3D patterns all consistently evolve to S1 at late time, irrespective of mesh resolution (Table 2).

An interesting observation is that the transient 3D fingering patterns are all combinations of the S1, S2, and S3 patterns observed in the 2D Elder problem (Figure 11). Based on this observation, we suggest that the 3D finger patterns must correspond to S1, S4, S5, S6, S7, S8 or S9, as only these patterns can be created by combining the S1, S2 and S3 patterns in 2D. Except for the S9 pattern, none of the 3D patterns is unique; for example, S6 may manifest in different ways, as schematically illustrated in Figure 12. Figure 12a shows an S6 pattern observed in our simulations, which involves one S1, three S2 and three S3 2D patterns. Figure 12b shows one S1 pattern, along with one S2 and three S3 patterns. Figure 12c involves four S2 and two S3 2D patterns. Finally, Figure 12d shows five S2 and two S3 2D patterns.

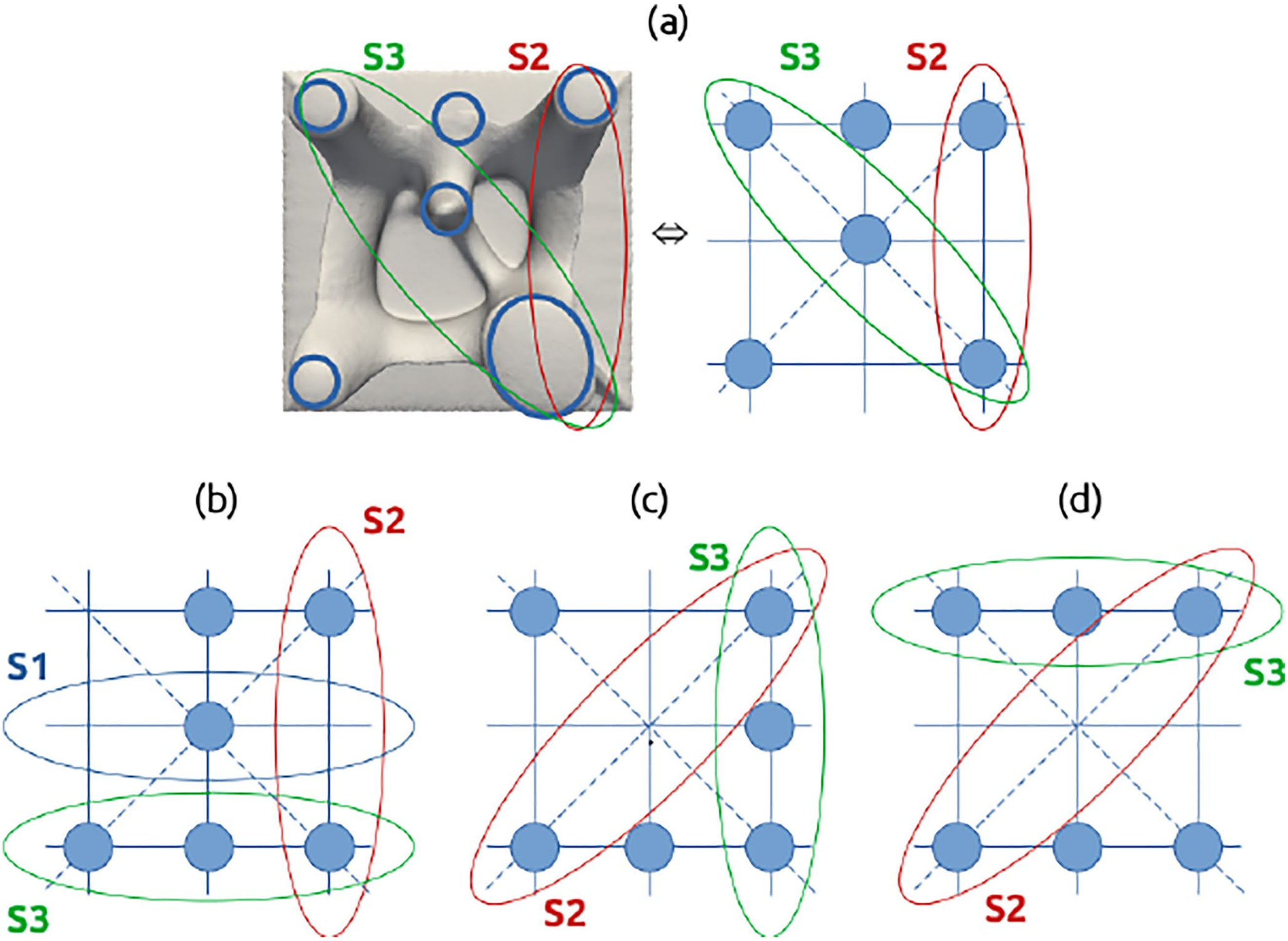

Figure 12. Snapshot of (a) the S6 3D fingering pattern from Figure 11 and its schematic representation; (b–d) show schematics of other S6 patterns.

We suggest that the absence of perfect symmetry of the transient 3D fingering patterns solutions is related to the use of an unstructured mesh with DMO: because the $Ra = 400$ Elder problem has a tendency to grow instabilities that originate from small perturbations, the solution is prone to deviate to one side or another of the domain depending on the local orientation of the tetrahedra (triangles in 2D) of the unstructured mesh and how this changes during DMO.

3.5. Application of DMO: 3D Salt Fingering in a Large-Scale Domain, $Ra = 1{,}200$

As a final demonstration of the advantages of DMO for unstable density-driven flow simulations, a very unstable, 3D salt fingering problem at $Ra = 1{,}200$ in a large-scale domain is simulated. The domain is enlarged by a factor of 10 in comparison to the Elder problem and therefore has a $6 \times 6 \times 1.5$ km geometry. A Rayleigh number of 1,200 is achieved by reducing the $Ra = 400$ Elder problem diffusivity and top boundary concentration by a factor of $\times 3$ and $\times 10$, respectively. The model represents a layer of saline groundwater overlying a freshwater layer, which is often encountered in subsurface aquifers. The density contrast causes convective salt fingers to develop and generates physical instabilities. In this case, the simulation using DMO requires approximately 9.4 million elements, while at least 50 million elements would have been necessary using a fixed mesh.

Here, no fingering trends are expected. Figure 13 shows the time evolution of the concentration $c = 0.05$ iso-contours together with the corresponding dynamic meshes. DMO captures the very numerous and unstable fingers at high resolution, coarsening the mesh where high resolution is not required. This demonstrates the practical utility of our approach and paves the way for real-scale, density-driven flow simulations.

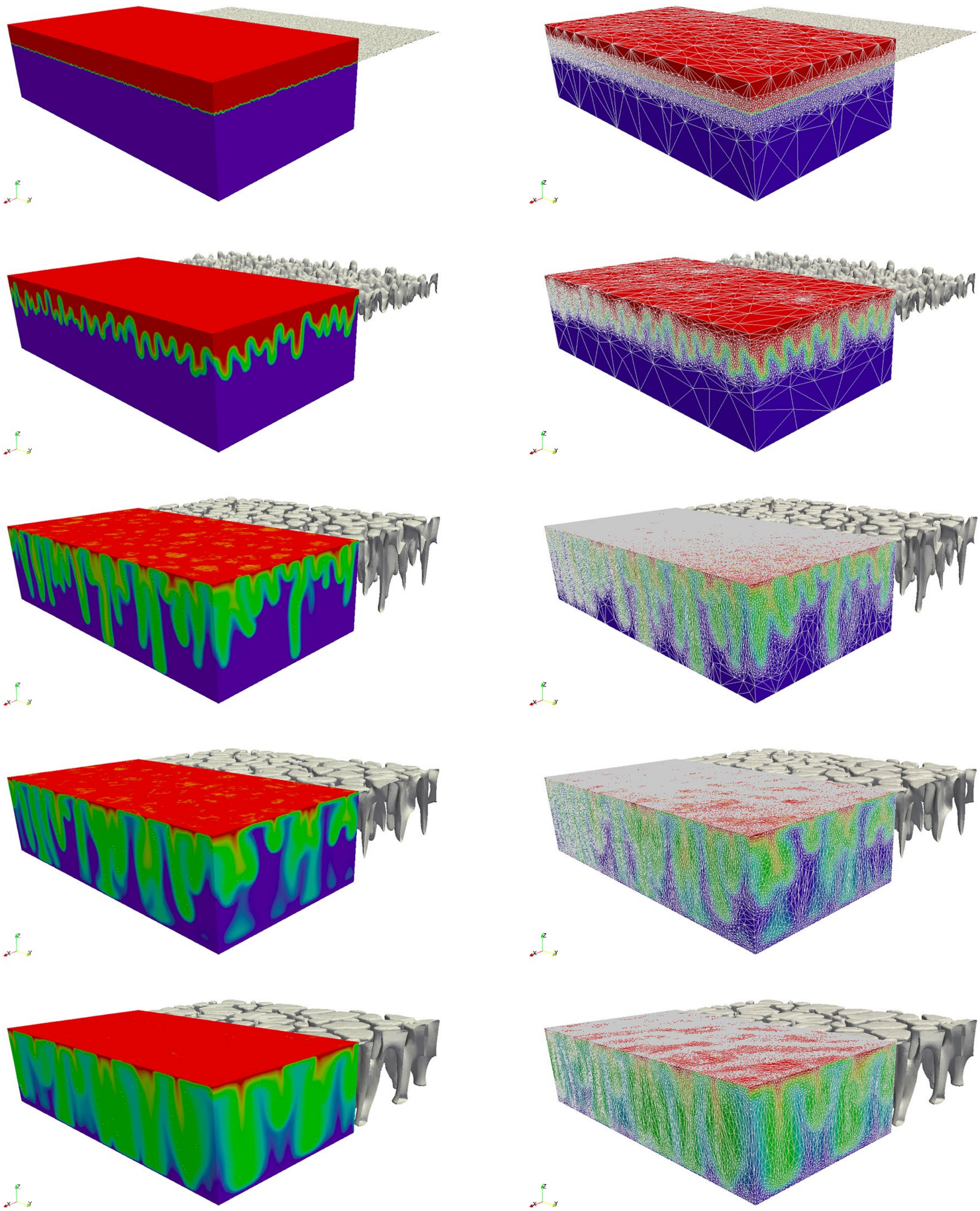

Figure 13. Time evolution of the salt concentration and associated adaptive mesh for the $Ra = 1{,}200$ 3D salt fingering problem in a large-scale ($6 \times 6 \times 1.5$ km) domain. The gray volumetric shape represents the $c = 0.05$ iso-contour.

4. Conclusions

We have investigated the use of fully unstructured meshes and dynamic mesh optimization to simulate density-driven flows using a double control finite element method. The main novelty of the work is twofold: (a) to demonstrate the significant computational speed-up obtained by using DMO in comparison to an equivalent fixed mesh, using the classical 2D Elder problem as a test case and (b) to apply the approach to model a 3D implementation of the Elder problem, demonstrating fingering patterns that have not been observed previously.

10.1029/2022WR032307

Benchmarking of the approach against solutions for the stable 2D purely diffusive and low Rayleigh number cases demonstrates that DMO can accurately reproduce the unique solutions for these cases, showing excellent computational speedup in comparison to using a fixed mesh, with DMO reducing simulation time by a factor in excess of ×13 for the finest mesh resolution tested.

For the unstable, high Rayleigh number case ($Ra = 400$), multiple steady-state solutions exist, referred to as "'S1," "S2," and "S3" based on the number of fingers (or plumes) appearing at steady-state. All three fingering patterns are obtained by the numerical approach used here, depending on the chosen mesh resolution, the timestep and/or the initial condition, consistent with previous studies. The approach includes velocity dependent dispersion and we show that dispersion has a negligible impact on the solutions, supporting the approach of numerous previous studies in which dispersion was omitted.

In this case, DMO reduces simulation time by a factor in excess of ×6 compared to an equivalent fixed mesh for the finest resolution tested. The speed-up offered by DMO increases as the number of elements in the fixed mesh increases.

Finally, the 2D $Ra = 400$ Elder problem has been extended to a 3D configuration. DMO here allowed simulation of a model that would require in excess of 50 million elements if discretized using a fixed mesh of equivalent resolution. The 3D Elder problem produced the S1 solution observed in 2D but also, at early times, new 3D fingering patterns, comprising S4, S5, S6, S7, S8, and S9. These early time, 3D finger patterns represent various combinations of the stable S1, S2 and S3 patterns observed previously in 2D. However, the large finger numbers are all transient and the late-time 3D solution consistently evolves to S1. We suggest that the stable S3 and S2 solutions to the Elder problem observed in 2D are an artifact of the reduced model dimensionality and that the only stable solution for the 3D Elder problem as configured here is S1. However, we tested only homogeneous initial conditions for the 3D case. It remains possible that using different initial conditions could lead to other steady-state solutions.

We conclude that DMO allows accurate simulation of unstable, density-driven flows in large 3D model domains at significantly lower computational cost than equivalent fixed meshes. The use of DMO with more accurate unstructured grids facilitates the numerical simulation of such flows in natural subsurface aquifers and reservoirs.

Data Availability Statement

The open-source IC-FERST software is available at http://multifluids.github.io/. The data files used for the simulations are available at https://zenodo.org/record/6779077%23.YrxUDnjMJ9k.

Acknowledgments
This work was supported by the UK Natural Environment Research Council (NERC) via the CuBES (Copper Basin Exploration Science) project (grant NE/T003294/1).

References

Abushaikha, A. S., Voskov, D. V., & Tchelepi, H. A. (2017). Fully implicit mixed-hybrid finite-element discretization for general purpose subsurface reservoir simulation. *Journal of Computational Physics*, *346*, 514–538. https://doi.org/10.1016/j.jcp.2017.06.034

Ackerer, P., & Younes, A. (2008). Efficient approximations for the simulation of density driven flow in porous media. *Advances in Water Resources*, *31*(1), 15–27. https://doi.org/10.1016/j.advwatres.2007.06.001

Adam, A., Pavlidis, D., Percival, J. R., Salinas, P., Xie, Z., Fang, F., et al. (2016). Higher-order conservative interpolation between control-volume meshes: Application to advection and multiphase flow problems with dynamic mesh adaptivity. *Journal of Computational Physics*, *321*, 512–531. https://doi.org/10.1016/j.jcp.2016.05.058

Anderson, D. G. (1965). Iterative procedures for nonlinear integral equations. *Journal of the ACM*, *12*(4), 547–560. https://doi.org/10.1145/321296.321305

Aristodemou, E., Boganegra, L. M., Mottet, L., Pavlidis, D., Constantinou, A., Pain, C., et al. (2018). How tall buildings affect turbulent air flows and dispersion of pollution within a neighbourhood. *Environmental Pollution*, *233*, 782–796. https://doi.org/10.1016/j.envpol.2017.10.041

Croucher, A. E., & O'Sullivan, M. J. (1995). The Henry problem for saltwater intrusion. *Water Resources Research*, *31*(7), 1809–1814. https://doi.org/10.1029/95wr00431

Dahle, H., Espedal, M., Ewing, R., & Sævereid, O. (1990). Characteristic adaptive subdomain methods for reservoir flow problems. *Numerical Methods for Partial Differential Equations*, *6*(4), 279–309. https://doi.org/10.1002/num.1690060402

Dahle, H., Espedal, M., Ewing, R., & Sævereid, O. (1992). Characteristic, local grid refinement techniques for reservoir flow problems. *International Journal of Numerical Engineering*, *34*(3), 1051–1069. https://doi.org/10.1002/nme.1620340324

Diersch, H.-J., & Kolditz, O. (2002). Variable-density flow and transport in porous media: Approaches and challenges. *Advances in Water Resources*, *25*(8–12), 899–944. https://doi.org/10.1016/s0309-1708(02)00063-5

Durlofsky, L. J. (1993). A triangle based mixed finite element—Finite volume technique for modeling two phase flow through porous media. *Journal of Computational Physics*, *105*(2), 252–266. https://doi.org/10.1006/jcph.1993.1072

Elder, J. W. (1967). Transient convection in a porous medium. *Journal of Fluid Mechanics*, *27*(3), 609–623. https://doi.org/10.1017/s0022112067000576

Elder, J. W., Simmons, C. T., Diersch, H.-J., Frolkovič, P., Holzbecher, E., & Johannsen, K. (2017). The Elder problem. *Fluids*, *2*(1), 11. https://doi.org/10.3390/fluids2010011

Farrell, P. E., & Maddison, J. R. (2011). Conservative interpolation between volume meshes by local Galerkin projection. *Computer Methods in Applied Mechanics and Engineering*, *200*(1–4), 89–100. https://doi.org/10.1016/j.cma.2010.07.015

Forsyth, P. A. (1991). A control volume finite element approach to NAPL groundwater contamination. *SIAM Journal on Scientific and Statistical Computing*, *12*(5), 1029–1057. https://doi.org/10.1137/0912055

Frolkovič, P., & De Schepper, H. (2000). Numerical modelling of convection dominated transport coupled with density driven flow in porous media. *Advances in Water Resources*, *24*(1), 63–72. https://doi.org/10.1016/s0309-1708(00)00025-7

Geiger, S., Roberts, S., Matthäi, S. K., Zoppou, C., & Burri, A. (2004). Combining finite element and finite volume methods for efficient multiphase flow simulations in highly heterogeneous and structurally complex geologic media. *Geofluids*, *4*(4), 284–299. https://doi.org/10.1111/j.1468-8123.2004.00093.x

Gomes, J. L. M. A., Pavlidis, D., Salinas, P., Xie, Z., Percival, J. R., Melnikova, Y., et al. (2017). A force-balanced control volume finite element method for multi-phase porous media flow modelling. *International Journal for Numerical Methods in Fluids*, *83*(5), 431–445. https://doi.org/10.1002/fld.4275

Hamzehloo, A., Bahlali, M. L., Salinas, P., Jacquemyn, C., Pain, C. C., Butler, A. P., & Jackson, M. D. (2021). Modelling saline intrusion using dynamic mesh optimization with parallel processing. *Water Resources Research*. (under review).

Helmig, R., & Huber, R. (1998). Comparison of galerkin-type discretization techniques for two-phase flow in heterogeneous porous media. *Advances in Water Resources*, *21*(8), 697–711. https://doi.org/10.1016/s0309-1708(97)00023-7

Hornung, R., & Trangenstein, J. (1997). Adaptive mesh refinement and multilevel iteration for flow in porous media. *Journal of Computational Physics*, *136*(2), 522–545. https://doi.org/10.1006/jcph.1997.5779

Jackson, M. D., Percival, J., Mostaghimi, P., Tollit, B., Pavlidis, D., Pain, C., et al. (2015). Reservoir modeling for flow simulation by use of surfaces, adaptive unstructured meshes, and an overlapping-control-volume finite-element method. *SPE Reservoir Evaluation and Engineering*, *18*(02), 115–132. https://doi.org/10.2118/163633-PA

Johannsen, K. (2002). The elder problem—Bifurcations and steady state solutions. In *Developments in Water Science* (Vol. 47, pp. 485–492). Elsevier.

Johannsen, K. (2003). On the validity of the Boussinesq approximation for the Elder problem. *Computational Geosciences*, *7*(3), 169–182. https://doi.org/10.1023/a:1025515229807

Kampitsis, A. E., Adam, A., Salinas, P., Pain, C. C., Muggeridge, A. H., & Jackson, M. D. (2020). Dynamic adaptive mesh optimisation for immiscible viscous fingering. *Computational Geosciences*, *24*(3), 1221–1237. https://doi.org/10.1007/s10596-020-09938-5

Künze, R. (2014). *Multiscale descriptions of density-driven flow instabilities in porous media* (Unpublished doctoral dissertation). Université de Lausanne, Faculté des géosciences et de l'environnement.

Künze, R., & Lunati, I. (2012). An adaptive multiscale method for density-driven instabilities. *Journal of Computational Physics*, *231*(17), 5557–5570. https://doi.org/10.1016/j.jcp.2012.02.025

Lunati, I., & Jenny, P. (2008). Multiscale finite-volume method for density-driven flow in porous media. *Computational Geosciences*, *12*(3), 337–350. https://doi.org/10.1007/s10596-007-9071-9

Mostaghimi, P., Kamali, F., Jackson, M. D., Muggeridge, A. H., & Pain, C. C. (2016). Adaptive mesh optimization for simulation of immiscible viscous fingering. *SPE Journal*, *21*(06), 2–250. https://doi.org/10.2118/173281-PA

Mostaghimi, P., Percival, J. R., Pavlidis, D., Ferrier, R. J., Gomes, J. L. M. A., Gorman, G. J., et al. (2015). Anisotropic mesh adaptivity and control volume finite element methods for numerical simulation of multiphase flow in porous media. *Mathematical Geosciences*, *47*(4), 417–440. https://doi.org/10.1007/s11004-014-9579-1

Mostaghimi, P., Tollit, B. S., Neethling, S. J., Gorman, G. J., & Pain, C. C. (2014). A control volume finite element method for adaptive mesh simulation of flow in heap leaching. *Journal of Engineering Mathematics*, *87*(1), 111–121. https://doi.org/10.1007/s10665-013-9672-3

Obeysekara, A., Lei, Q., Salinas, P., Pavlidis, D., Xiang, J., Latham, J.-P., & Pain, C. (2018). Modelling stress-dependent single and multi-phase flows in fractured porous media based on an immersed-body method with mesh adaptivity. *Computers and Geotechnics*, *103*, 229–241. https://doi.org/10.1016/j.compgeo.2018.07.009

Pain, C. C., Umpleby, A. P., De Oliveira, C. R. E., & Goddard, A. J. H. (2001). Tetrahedral mesh optimisation and adaptivity for steady-state and transient finite element calculations. *Computer Methods in Applied Mechanics and Engineering*, *190*(29–30), 3771–3796. https://doi.org/10.1016/S0045-7825(00)00294-2

Papaspyros, J. N. E., Moutsopoulos, K. N., & Tzavellas, E. (2016). Solutions of the elder problem for a wide range of the Rayleigh number. *European Water*, *55*, 31–40.

Park, C.-H., & Aral, M. M. (2007). Sensitivity of the solution of the Elder problem to density, velocity and numerical perturbations. *Journal of Contaminant Hydrology*, *92*(1–2), 33–49. https://doi.org/10.1016/j.jconhyd.2006.11.008

Piggott, M. D., Farrell, P. E., Wilson, C. R., Gorman, G. J., & Pain, C. C. (2009). Anisotropic mesh adaptivity for multi-scale ocean modelling. *Philosophical Transactions of the Royal Society A: Mathematical, Physical & Engineering Sciences*, *367*(1907), 4591–4611. https://doi.org/10.1098/rsta.2009.0155

Prasad, A., & Simmons, C. T. (2003). Unstable density-driven flow in heterogeneous porous media: A stochastic study of the Elder [1967b] "short heater" problem. *Water Resources Research*, *39*(1), SBH 4-1–SBH 4-21. https://doi.org/10.1029/2002wr001290

Salinas, P., Pavlidis, D., Xie, Z., Adam, A., Pain, C. C., & Jackson, M. D. (2017). Improving the convergence behaviour of a fixed-point-iteration solver for multiphase flow in porous media. *International Journal for Numerical Methods in Fluids*, *84*(8), 466–476. https://doi.org/10.1002/fld.4357

Salinas, P., Pavlidis, D., Xie, Z., Jacquemyn, C., Melnikova, Y., Jackson, M. D., & Pain, C. C. (2017). Improving the robustness of the control volume finite element method with application to multiphase porous media flow. *International Journal for Numerical Methods in Fluids*, *85*(4), 235–246. https://doi.org/10.1002/fld.4381

Salinas, P., Pavlidis, D., Xie, Z., Osman, H., Pain, C. C., & Jackson, M. D. (2018). A discontinuous control volume finite element method for multi-phase flow in heterogeneous porous media. *Journal of Computational Physics*, *352*, 602–614. https://doi.org/10.1016/j.jcp.2017.09.058

Salinas, P., Regnier, G., Jacquemyn, C., Pain, C. C., & Jackson, M. D. (2021). Dynamic mesh optimisation for geothermal reservoir modelling. *Geothermics*, *94*, 102089. https://doi.org/10.1016/j.geothermics.2021.102089

Schmidt, G., & Jacobs, F. (1988). Adaptive local grid refinement and multi-grid in numerical reservoir simulation. *Journal of Computational Physics*, *77*(1), 140–165. https://doi.org/10.1016/0021-9991(88)90160-x

Thorne, D. T., & Sukop, M. C. (2004). Lattice Boltzmann model for the Elder problem. In *Developments in Water Science* (Vol. 55, pp. 1549–1557). Elsevier.

Trangenstein, J. (2002). Multi-scale iterative techniques and adaptive mesh refinement for flow in porous media. *Advances in Water Resources*, *25*(8–12), 1175–1213. https://doi.org/10.1016/s0309-1708(02)00053-2

10.1029/2022WR032307

Van Reeuwijk, M., Mathias, S. A., Simmons, C. T., & Ward, J. D. (2009). Insights from a pseudospectral approach to the Elder problem. *Water Resources Research*, *45*(4). https://doi.org/10.1029/2008wr007421

Viré, A., Xiang, J., Milthaler, F., Farrell, P. E., Piggott, M. D., Latham, J.-P., et al. (2012). Modelling of fluid–solid interactions using an adaptive mesh fluid model coupled with a combined finite–discrete element model. *Ocean Dynamics*, *62*(10–12), 1487–1501. https://doi.org/10.1007/s10236-012-0575-z

Voss, C. I., & Souza, W. R. (1987). Variable density flow and solute transport simulation of regional aquifers containing a narrow freshwater-saltwater transition zone. *Water Resources Research*, *23*(10), 1851–1866. https://doi.org/10.1029/wr023i010p01851

Wolff, M., Flemisch, B., & Helmig, R. (2013). An adaptive multiscale approach for modeling two-phase flow in porous media including capillary pressure. *Water Resources Research*, *49*(12), 8139–8159. https://doi.org/10.1002/2013wr013800

Woods, J. A., & Carey, G. F. (2007). Upwelling and downwelling behavior in the Elder-Voss-Souza benchmark. *Water Resources Research*, *43*(12), W12403. https://doi.org/10.1029/2006wr004918

Woods, J. A., Teubner, M. D., Simmons, C. T., & Narayan, K. A. (2003). Numerical error in groundwater flow and solute transport simulation. *Water Resources Research*, *39*(6), 1158. https://doi.org/10.1029/2001wr000586

Xie, Z., Pavlidis, D., Salinas, P., Percival, J. R., Pain, C. C., & Matar, O. K. (2016). A balanced-force control volume finite element method for interfacial flows with surface tension using adaptive anisotropic unstructured meshes. *Computers & Fluids*, *138*, 38–50. https://doi.org/10.1016/j.compfluid.2016.08.005

Yang, P., Xiang, J., Fang, F., Pavlidis, D., Latham, J.-P., & Pain, C. C. (2016). Modelling of fluid–structure interaction with multiphase viscous flows using an immersed-body method. *Journal of Computational Physics*, *321*, 571–592. https://doi.org/10.1016/j.jcp.2016.05.035

Younes, A., & Ackerer, P. (2010). Empirical versus time stepping with embedded error control for density-driven flow in porous media. *Water Resources Research*, *46*(8). https://doi.org/10.1029/2009wr008229

Zheng, J., Zhu, J., Wang, Z., Fang, F., Pain, C. C., & Xiang, J. (2015). Towards a new multiscale air quality transport model using the fully unstructured anisotropic adaptive mesh technology of fluidity (version 4.1. 9). *Geoscientific Model Development*, *8*(10), 3421–3440. https://doi.org/10.5194/gmd-8-3421-2015